

New results on the gamma-ray burst variability–luminosity relation[★]

C. Guidorzi^{★,★,1,2,3}, R. Maccary^{1,3}, A. Tsvetkova^{4,5}, S. Kobayashi⁶, L. Amati³, L. Bazzanini^{1,3},
M. Bulla^{1,2,7}, A. E. Camisasca⁸, L. Ferro^{1,3}, D. Frederiks⁵, F. Frontera^{1,3}, A. Lysenko⁵, M. Maistrello^{1,3},
A. Ridnaia⁵, D. Svinkin⁵, and M. Ulanov⁵

¹ Department of Physics and Earth Science, University of Ferrara, Via Saragat 1, I-44122 Ferrara, Italy

² INFN – Sezione di Ferrara, Via Saragat 1, 44122 Ferrara, Italy

³ INAF – Osservatorio di Astrofisica e Scienza dello Spazio di Bologna, Via Piero Gobetti 101, 40129 Bologna, Italy

⁴ Department of Physics, University of Cagliari, SP Monserrato-Sestu, km 0.7, 09042 Monserrato, Italy

⁵ Ioffe Institute, Politekhnikeskaya 26, 194021 St. Petersburg, Russia

⁶ Astrophysics Research Institute, Liverpool John Moores University, Liverpool Science Park IC2, 146 Brownlow Hill, Liverpool, L3 5RF, UK

⁷ INAF, Osservatorio Astronomico d’Abruzzo, via Mentore Maggini snc, 64100 Teramo, Italy

⁸ Astronomical Observatory of the Autonomous Region of the Aosta Valley (OAVdA), Loc. Lignan 39, I-11020, Nus (Aosta Valley), Italy

September 5, 2024

ABSTRACT

Context. At the dawn of the gamma-ray burst (GRB) afterglow era, a Cepheid-like correlation was discovered between time variability V and isotropic-equivalent peak luminosity L_{iso} of the prompt emission of about a dozen long GRBs with measured redshift available at that time. Soon afterwards, the correlation was confirmed against a sample of about 30 GRBs, despite being affected by significant scatter. Unlike the minimum variability timescale (MVT), V measures the relative power of short-to-intermediate timescales.

Aims. We aim to test the correlation using about two hundred long GRBs with spectroscopically measured redshift, detected by *Swift*, *Fermi*, and *Konus/WIND*, for which both observables can be accurately estimated.

Methods. For all the selected GRBs, variability was calculated according to the original definition using the 64-ms background-subtracted light curves of *Swift*/BAT (*Fermi*/GBM) in the 15–150 (8–900) keV energy passband. Peak luminosities were either taken from literature or derived from modelling broad-band spectra acquired with either *Konus/WIND* or *Fermi*/GBM.

Results. The statistical significance of the correlation has weakened to $\lesssim 2\%$, mostly due to the appearance of a number of smooth and luminous GRBs characterised by a relatively small V . At odds with most long GRBs, 3 out of 4 long-duration merger candidates have high V and low L_{iso} .

Conclusions. Luminosity is more tightly connected with shortest timescales measured by MVT rather than short-to-intermediate ones, measured by V . We discuss the implications on internal dissipation models and the role of the e^\pm photosphere. We identified a few, smooth GRBs with a single broad pulse and low V , that might have an external shock origin, in contrast with most GRBs. The combination of high variability ($V \gtrsim 0.1$), low luminosity $L_{\text{iso}} \lesssim 10^{51}$ erg s⁻¹ and short MVT ($\lesssim 0.1$ s) could be a good indicator for a compact binary merger origin.

Key words. (Stars:) Gamma-ray burst: general – Methods: statistical

1. Introduction

In the early days of multi-messenger and time-domain astrophysics and big surveys, the number and diversity of explosive transients are rapidly increasing and are expected to continue doing so in the coming years. In this context, gamma-ray bursts (GRBs) remain central to the field, due to the expanding sample of electromagnetic detections at TeV energies (see [Nava 2021](#); [Noda & Parsons 2022](#) for reviews), their association with gravitational waves (GWs; [Abbott et al. 2017](#)), and their potential as sources of high-energy neutrinos (see [Mészáros 2017](#); [Murase & Bartos 2019](#); [Kimura 2023](#) for reviews).

Since their first discovery, the wealth of information encoded in GRB prompt emission light curves (LCs) has provided valuable insights, ranging from the classification of progenitors to constraints on the dissipation mechanism and radii. Regarding the progenitors, short GRBs signal the merger of a compact object binary system ([Blinnikov et al. 1984](#); [Eichler et al. 1989](#); [Paczynski 1991](#); [Narayan et al. 1992](#); [Abbott et al. 2017](#)), while long GRBs indicate the core collapse of certain massive stars also known as “collapsar” ([Woosley 1993](#); [Paczynski 1998](#); [MacFadyen & Woosley 1999](#); [Yoon & Langer 2005](#)). Although recent cases have shown that duration alone can be misleading, other indicators related to the temporal properties of the prompt emission may aid in their identification ([Camisasca et al. 2023a](#); [Veres et al. 2023](#)).

At the dawn of the afterglow era, the diversity and complexity of long GRB LCs led to the development of various metrics to

[★] Tables 2 to 3 are only available in electronic form at the CDS via anonymous ftp to cdsarc.u-strasbg.fr (130.79.128.5) or via <http://cdsweb.u-strasbg.fr/cgi-bin/qcat?J/A+A/>

^{★★} guidorzi@fe.infn.it

quantify their variability. The common goal was to evaluate how a given LC fluctuates around a smoothed version of itself, emphasising the relative power of short-to-intermediate timescales compared to long ones (Fenimore & Ramirez-Ruiz 2000; Reichart et al. 2001, hereafter R01). The rationale was that the power associated with the shortest timescales (down to a few tens and only rarely to ms, Golkhou et al. 2015), which modulates the profiles of long and very long GRBs without apparent evolution, supports an internal dissipation mechanism rather than external shocks, which dominate the afterglow emission (Fenimore et al. 1999).

Once the redshifts of the first long GRBs were determined, R01 identified a correlation between variability V and peak isotropic-equivalent luminosity L_{iso} for a dozen GRBs with measurable quantities: $L_{\text{iso}} \propto V^\alpha$ with $\alpha = 3.3^{+1.1}_{-0.9}$. A similar result, based on a slightly different definition of V , was reported by Fenimore & Ramirez-Ruiz (2000), using a smaller sample. Adopting the R01 definition of V , this correlation was confirmed a few years later in a sample of about 30 GRBs, despite considerable scatter (Guidorzi et al. 2005, hereafter G05) and ongoing debate about the exact value of α (Guidorzi et al. 2006).

During the *Neil Gehrels Swift* Observatory (Gehrels et al. 2004) and *Fermi* era, research shifted to a different temporal metric, known as the minimum variability timescale (MVT; MacLachlan et al. 2012, 2013; Golkhou & Butler 2014; Golkhou et al. 2015). MVT identifies the shortest timescale over which a significant flux change occurs in an uncorrelated way, indicating a different temporal structure from the surrounding bins. It was found that MVT is anti-correlated with the bulk Lorentz factor Γ measured from the afterglow onset time, following a relation $\text{MVT} \propto \Gamma^{-\beta}$, with β values ranging from 2 to 4, depending on the exact definition of MVT and the GRB sample (Sonbas et al. 2015; Camisasca et al. 2023a). Additionally, MVT was observed to anti-correlate with L_{iso} , after accounting for the selection effects (Camisasca et al. 2023a).

Interpreting the observed variability as a result of internal dissipation processes, the e^\pm photosphere would smooth out all dissipation events occurring below its radius, thereby determining the observed MVT (Kobayashi et al. 2002; Mészáros et al. 2002). In a model involving a wind of shells with varying emission times and Lorentz factors Γ , smaller values of Γ would correspond to smaller dissipation radii and thus potentially experience stronger smoothing effects from the e^\pm photosphere. This implies that slower shells would result in longer MVT. The V - L_{iso} correlation was interpreted as arising from a correlation between the jet's opening angle and the mass of the relativistic ejecta (Kobayashi et al. 2002), under the assumption that the collimation-corrected gamma-ray released energy was narrowly clustered, although it was later found to be more broadly distributed than initially thought (Liang et al. 2008).

Twenty years have passed since the last tests of the V - L_{iso} correlation. Today, with nearly ten times more GRBs available with suitable data for measuring both V and L_{iso} , thanks to catalogues like *Swift*, *Fermi*, and *Konus/WIND*, we can re-examine this relation with greater statistical sensitivity. The goals of the present work are twofold: (i) to conduct an updated and more statistically sensitive test of the V - L_{iso} relation using these extensive GRB catalogues and (ii) to explore for the first time the relation between V and MVT, metrics often vaguely interpreted as similar measures for variability or assumed to be strongly correlated.

Section 2 describes the data sets, with their analysis detailed in Section 3. The results are presented in Section 4 and discussed in Section 5, followed by the conclusions in Section 6. Through-

out this paper, we assume the latest Planck cosmological parameters: $H_0 = 67.4 \text{ km s}^{-1} \text{ Mpc}^{-1}$, $\Omega_m = 0.315$, $\Omega_\Lambda = 0.685$ (Planck Collaboration et al. 2020).

2. Data sets

2.1. *Swift*/BAT sample

We selected all the long GRBs detected by *Swift*/BAT in burst mode from January 2005 to February 2024 with measured spectroscopic redshift and rejected all the events that had been classified as either short or short with extended emission (Norris & Bonnell 2006), whereas the long-lasting merger candidates GRB 060614, GRB 191019A¹, and GRB 211211A (Gehrels et al. 2006; Levan et al. 2023; Yang et al. 2022) were treated separately. The information on the classification of each GRB was taken either from the BAT3 catalogue (Lien et al. 2016), when available, or from the *Swift*/BAT team circulars. We also rejected the bursts whose LCs had not entirely been covered in burst mode, or which were affected by data gaps during the GRB. All the bursts, for which no information was accessible on the time-integrated, *broad-band* spectrum apart from the one in the 15–150 keV band obtained by BAT itself, were discarded: being interested in a reliable estimate of the bolometric peak luminosity, we considered the BAT spectrum alone inadequate because of its narrow passband, which in most cases cannot constrain the peak energy of the νF_ν spectrum and/or the high-energy index.²

For each burst with redshift z , following the guidelines of the BAT team³, we extracted the mask-weighted LCs in the 15–150 keV passband with six different bin times, $\Delta t = 64(1+z)^\beta$ ms, with β ranging from 0 to 1 and evenly spaced by 0.2 increments. As it is clarified later on, this is a way to obtain all the LCs with a common bin time in the *comoving* frame, accounting for both cosmological time dilation and the dependence of GRB time profiles on photons' energy. As a result, we ended up with a sample of 278 GRBs from *Swift*/BAT.

2.2. *Fermi*/GBM sample

From the catalogue of long GRBs provided by the *Fermi* team, we selected all the long ($T_{90} > 2$ s) GRBs from July 14, 2008 to February 4, 2024 with spectroscopically measured redshift. Long-duration merger candidates GRB 211211A and GRB 230307A (Troja et al. 2022; Gompertz et al. 2023; Dichiaro et al. 2023; Levan et al. 2024) were treated separately, as we did for the BAT sample. We also ignored the few, very bright GRBs which saturated the GBM detectors, such as GRB 130427A and GRB 221009A (Preece et al. 2014; Lesage et al. 2023). We rejected the GRBs that are affected by the simultaneous occurrence of a solar flare or whose profile was not entirely covered by the time-tagged event (TTE) mode of GBM.

For each GRB the LCs of the most illuminated NaI detectors were extracted in three different energy bands: 8–150, 150–900, and 8–900 keV energy range. Regarding the LC bin times, we adopted the same strategy as for the BAT data: six different values, $\Delta t = 64(1+z)^\beta$ ms, where z is the redshift and β varies from 0 and 1. Background was interpolated and subtracted using the

¹ An alternative interpretation as a disguised tidal disruption event was also put forward for this event (Eyles-Ferris et al. 2024).

² We made an exception for 191019A, given the interest in this merger candidate along with the possibility of constraining the peak energy.

³ https://swift.gsfc.nasa.gov/analysis/threads/bat_threads.html.

GBM data tools⁴ (Goldstein et al. 2022) following standard prescriptions (see Maccary et al. 2024a for details). For each burst we chose the GBM detectors based on the “scat detector mask” entry on the HEASARC catalogue⁵. We used the TTE data from the start of its T_{90} interval to the end.

Charged particle spikes were identified and removed from the LCs as follows: whenever counts in a bin exceeded by $\geq 9\sigma$ the adjacent bins, they were tagged as due to a potential spike. If visual inspection of different GBM units confirmed the spurious nature of a possible spike by exhibiting completely different intensities, therefore incompatible with being caused by a plane electromagnetic wave, its counts were replaced with the mean of the adjacent bins.

In this way, we came up with a sample of 136 GRBs from *Fermi*/GBM.

3. Data analysis

3.1. Estimate of variability

For each GRB, we preliminarily determined the time window including the GRB signal, to be used for calculating the variability V_f ; f is the fraction of the total net counts, upon which the definition of variability depends in the way that is explained below. After a few attempts to find the best compromise between the need of covering the whole GRB profile and limiting the impact of noise, we opted for the following criterium: we determined the 7σ interval, whose boundaries correspond to the first and the last time bin in which the net count rate exceeds zero by $\geq 7\sigma$, where σ is the count rate error. This window was determined through the analysis of any given LC considering a range of bin times, from the original one to its multiples 2^n ($n = 1, 2, \dots, 7$).⁶ Hereafter, all the following steps will refer to the data within the 7σ window of each GRB. To limit the impact of low-S/N GRBs, we rejected all the bursts whose total net counts have $S/N < 30$.

Let (r_i, σ_i) be the net count rate and its Gaussian error relative to the i -th time bin. The Gaussian limit is ensured in the case of BAT mask-weighted profiles by the central limit theorem, being the result of linear combinations of numerous independent counters, whereas the typical counts in the bin times of GBM profiles adopted in this work are always enough.

Following R01, variability V_f is calculated as

$$V_f = \frac{\sum_{i=1}^n [(r_i - s_{f,i})^2 - k_f \sigma_i^2]}{\sum_{i=1}^n (r_i^2 - \sigma_i^2)}, \quad (1)$$

where n is the number of bins. $\{s_{f,i}\}$ is the smoothed version of the original LC $\{r_i\}$, obtained as the convolution of $\{r_i\}$ with a boxcar window with duration T_f . This, in turn, is defined as the shortest cumulative time collecting a fraction f of the total net counts. The interval defining T_f is not necessarily contiguous, as it may be the case in the presence of quiescent times (see figures 1 and 2 of R01); f is initially treated as a free parameter in the interval $[0.1, 0.9]$. The factor k_f corrects the weight of the noise variance to be subtracted and is calculated as $(1 - 1/n_f)$, where n_f is the number of bins within the smoothing boxcar window of duration T_f , thus equal to the rounded integer of $T_f/\Delta t$,

⁴ https://fermi.gsfc.nasa.gov/ssc/data/analysis/gbm/gbm_data_tools/gdt-docs/.

⁵ <https://heasarc.gsfc.nasa.gov/db-perl/W3Browse/w3table.pl?tablehead=name%3Dfermigbrst&Action=More+Options>

⁶ This ensures that long-lasting, weak but statistically significant tails may not be cut off.

where Δt is the bin time of the original LC. This factor comes from the fact that, in the numerator of Eq. (1), r_i and $s_{f,i}$ are not independent. The subscript f in the definition of V in Eq. (1) reminds us that it depends on f through the dependence of the smoothed version of the LC on f .

By construction, V_f ranges between 0 and 1. Both variance terms in the numerator and in the denominator of Eq. (1) are removed of the contribution due to statistical noise (σ_i^2).

The essence of the definition of V_f can be summarised in three main steps:

1. determining the characteristic smoothing time T_f as a function of f ;
2. determining the smoothed version $\{s_{f,i}\}$ of the original LC $\{r_i\}$; the subscript f reminds us that the smoothed profile depends on T_f , which, in turn, depends on f ;
3. estimating how the original LC fluctuates around the smoothed version obtained in 2., removing the contribution of the noise due to counting statistics.

To calculate T_f we had to preliminarily determine the optimal bin time for any given LC: a too fine value would lead to underestimating T_f because dominated by statistical fluctuations, whereas a rough resolution would cause a loss of sensitivity to the GRB temporal structures with consequent overestimate of T_f . The detection timescale of the narrowest, $\geq 5\sigma$ significant peak, as determined with MEPSA (Guidorzi 2015), was found to be the best bin time to estimate T_f in an unbiased way for all GRBs. Consequently, each LC was rebinned accordingly and then used only for the task of calculating T_f .

Equation (1) is a simplified version of the original equation of R01: thanks to the TTE data which allow us to accumulate LCs with the desired bin time, we need not smooth the original light curve as it was the case for the binned profiles used by R01 and G05. We tested Equation (1) by carrying out a suite of simulations, assuming light curves with negligible statistical uncertainties, for which V_f could therefore be calculated with negligible uncertainty. We then applied Equation (1) to a set of random noisy realisations of the same synthetic profiles and verified that we obtained unbiased and consistent values within uncertainties.

The error on V_f was calculated as follows: we assumed the original LC as the set of expected rates and we generated 1000 synthetic profiles, where each simulated rate $r_{\text{sim},i} \sim N(r_i, \sigma_i^2)$. In this way, we ended up with second-order realisations of the true (error-free and unknown) profile, so the corresponding variance of $r_{\text{sim},i}$ is $2\sigma_i^2$, not just σ_i^2 . Each synthetic profile went through the same three steps above and treated like the real LC. From the distribution of the simulated values of $V_{\text{sim},f}$ we obtained the 90% confidence interval, given by the 5% and 95% quantiles.

Figure 1 shows the example of the famous GRB 080319B LC (Racusin et al. 2008) measured by BAT along with its smoothed profile: for that GRB, assuming $f = 0.45$, it is found $T_f = 18.43 \pm 0.13$ s.

3.2. Estimate of peak luminosity

Firstly, we used estimates of L_{iso} derived from broad-band modeling for all BAT GRBs, for which they were already available in the literature. For BAT GRBs having both KW and GBM estimates, we systematically preferred KW (Tsvetkova et al. 2017, 2021), after making sure that they were consistent within uncertainties. The preference for KW relies in its better capability in constraining the high-energy power-law index, whereas GBM (NaI) is mainly limited by its smaller effective area above 100 keV (Tsvetkova et al. 2022). For the remaining

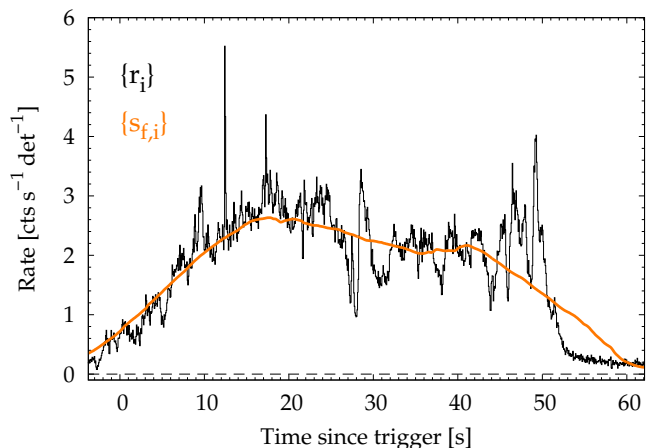


Fig. 1. Illustrative example of how variability is calculated. Shown is the 15–150-keV light curve $\{r_i\}$ of GRB 080319B as observed with BAT. The orange line shows the smoothed profile $\{s_{f,i}\}$ obtained with a smoothing timescale of $T_f = 18.43$ s, which collects a fraction $f = 0.45$ of the total fluence of the GRB.

BAT GRBs detected by KW, we adopted the same approach as in the KW catalogues: the isotropic luminosities were computed from the peak energy fluxes and k -corrected to the energy range $1/(1+z)$ keV–10 MeV.⁷ The peak spectrum was accumulated over a time interval T_p around the peak, which lasted longer than 64 ms to collect enough photons. Then, under the assumption of negligible spectral evolution during T_p , we rescaled the average flux resulted from fitting the spectrum by the ratio r_{64}/r_{T_p} , where r_{64} and r_{T_p} are respectively the peak count rate evaluated over 64 ms and the average count rate over T_p . Both count rates refer to the KW net counts in the ~ 20 –1200 keV light curves.

For the *Fermi* GRBs observed from the August 4, 2008 to June 20, 2018, we used the peak luminosity provided in the *Fermi* spectral catalogue (Poolakkil et al. 2021). For the remaining 40 more recent GBM bursts, the peak luminosity was computed as

$$L_{\text{iso,GBM}} = 4\pi d_L^2 k \phi_{p,8-900}, \quad (2)$$

where d_L is the luminosity distance, k the k -correction and $\phi_{p,8-900}$ the peak flux in the 8–900 keV energy range. The peak flux is computed from the best-fitting Band function of the spectrum accumulated over a 1.024-s window centred on the peak time and modelled with the GBM data tools. We made sure that our procedure yields consistent results with the ones published in Poolakkil et al. (2021) within 30% accuracy by independently analysing a few common GRBs. For 22/40 cases, as the high-energy spectral index of the Band function was poorly constrained, we fixed it to the typical value of -2.3 (Preece et al. 2000; Kaneko et al. 2006; Guidorzi et al. 2011; Tsvetkova et al. 2017). The k -correction was obtained by renormalising the peak flux in the $1/(1+z)$ – $10^4/(1+z)$ keV observer-frame energy band. For the final merged sample, for each GRB in common between KW and GBM, we opted for the L_{iso} estimate of the former.

Lastly, for the long-duration merger candidate GRB 191019A (Levan et al. 2023) only BAT data were available. We extracted the 15–150 keV spectrum at peak centred at 0.272 s since the trigger time with an exposure of 0.128 s, given by the detection timescale of MEPSA. Although a

⁷ As explained in Tsvetkova et al. (2017, 2021), using the rest-frame upper boundary of $10(1+z)$ MeV instead of 10 MeV compensates the fact that the *Konus/WIND* energy range extends to 10–25 MeV.

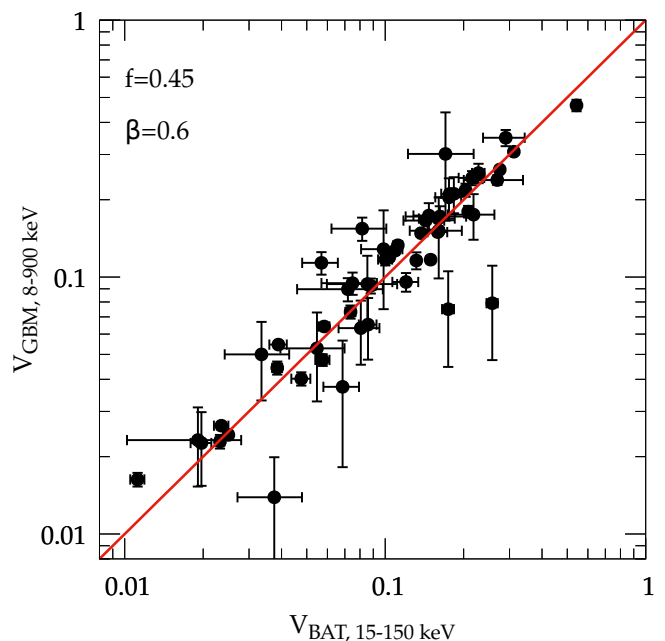


Fig. 2. Comparison between estimates of variability obtained with BAT in the 15–150 keV band vs. the GBM estimates in the 8–900 keV band, obtained for a common sample and assuming $f = 0.45$ and $\beta = 0.6$. Equality is shown by the solid line.

simple power-law yields an acceptable fit, the photon index of $\Gamma = 1.78 \pm 0.22$ is suggestive of the presence of the peak energy of the νF_ν spectrum, E_p within the BAT passband (Sakamoto et al. 2009). We therefore modelled it with the Band function (Band et al. 1993), fixing the low- and the high-energy indices to the typical values of -1 and -2.3 , respectively. We found $E_p = 62_{-20}^{+29}$ keV. Calculating the fluence in the 1 – 10^4 keV rest-frame band, the peak flux is $(1.2 \pm 0.2) \times 10^{-6}$ erg cm $^{-2}$ s $^{-1}$, corresponding to $L_{\text{iso}} = (2.6 \pm 0.5) \times 10^{50}$ erg s $^{-1}$.

4. Results

From the analysis of a common sample of BAT-GBM GRBs, for which significant measures of V_f were available for each of the three energy passbands (15–150, 8–150, and 150–900 keV), we found that in most cases there is a weak dependence of V_f on the energy passband and on the used detector. In practice, taking the two sets of V_f estimates obtained from the full passbands of each detector (15–150 vs. 8–900 keV, respectively), which conveniently have the best S/N, 85–90% of them differ by $\lesssim 20\%$. Figure 2 shows the comparison between the two estimates of V_f for the specific case of $f = 0.45$ and $\beta = 0.6$. A more comprehensive comparison and analysis is reported in Appendix A. To the aim of the present investigation, a $\lesssim 20\%$ mismatch in V_f can be neglected, as the dynamic range of V_f as well as the scatter observed in the V_f – L plane will show. Consequently, for the majority of GRBs we may neglect the dependence of V_f on the energy passbands, in agreement with what was found by R01.

For a common sample of 97 GRBs detected by *Konus/WIND* and *Fermi*/GBM, for which it was thus possible to independently estimate the 1 – 10^4 keV rest-frame L_{iso} , we compared the two sets of values. The two sets are overall consistent over more than three decades. The distribution of the ratio $L_{\text{iso,KW}}/L_{\text{iso,GBM}}$ presents a median value of 1.3 with [1.0, 1.6] as interquartile

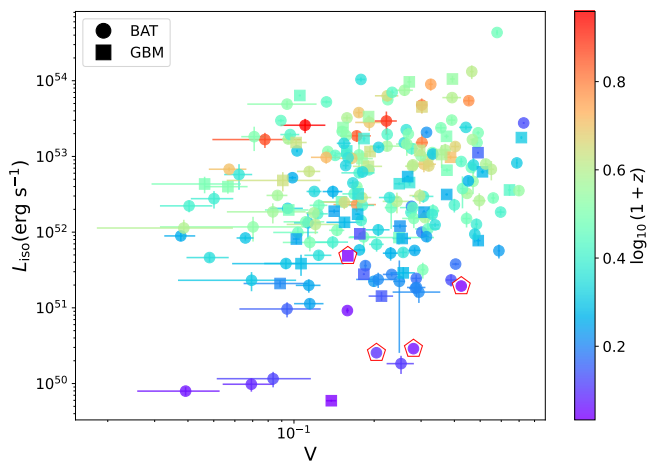


Fig. 3. Variability–luminosity correlation obtained for $f = 0.8$ and $\beta = 0.6$. This value of f gives the highest degrees of correlation. Different symbols refer to the different detectors used to measure V_f . For BAT–GBM shared GRBs we used BAT values. Pentagons are long-duration merger candidates. The redshift information is also available through the colour-coded scale.

range.⁸ That the KW estimate is $(30 \pm 30)\%$ higher stems from its better capability in constraining the high-energy PL index, already discussed in Section 3.2. KW estimates are therefore preferable and were used for the sample of common GRBs. Overall, for the GRBs detected by GBM alone, a 30% discrepancy has a negligible impact on the V_f – L correlation, as it is shown in the following.

4.1. Variability versus peak luminosity

It was originally found by R01 that the most significant correlation between V_f and L_{iso} is obtained for $f = 0.45$. β was fixed to 0.6, because of the contrasting effects due, on the one side, to cosmic dilation, which would demand $\beta = 1$, and, on the other side, to the narrowing of pulses with energy, which would instead imply $\beta = -0.4$ (see R01).

First of all, in the evaluation of the statistical significance of the V_f – L_{iso} correlation that follows, we ignored the four long-duration merger candidates and in the end we show them only for comparison.

We systematically calculated the correlation coefficients (Pearson’s r , Spearman’s ρ , Kendall’s τ) between $\log V_f$ and $\log L_{\text{iso}}$ for the entire grid of (f, β) values (Section 3). We explored $\beta \neq 0.6$ values for the sake of completeness. For any values of (f, β) we considered only the pairs (V_f, L_{iso}) with a $V_f > 0$ at 90% confidence; the remaining GRBs were simply ignored, because their 90% upper limits on V_f did not turn out to be usefully constraining in the V_f – L_{iso} plane. Consequently, the number of selected GRBs varies for different (f, β) values. Overall, the joint sample includes 216 GRBs with significant estimates for both observables: hereafter, this is referred to as the merged sample.

We first restrict ourselves to the $\beta = 0.6$ cases for the reasons explained above. The highest degree of correlation using Pearson’s r is found for $f = 0.8$ from a sample of 212 GRBs: the p-values associated with r , ρ , and τ are 3.1×10^{-4} , 4.9×10^{-3} , and 5.7×10^{-3} , respectively. The result is shown in Figure 3,

⁸ It is the range comprising the two central quartiles, so the 25–75 percentiles.

whose values are reported in Table 2. Alternatively, using non-parametric ρ and τ , the most significant case is obtained for $f = 0.9$ and 215 GRBs, with p-values that are comparable with the $f = 0.8$ case: 8.5×10^{-4} , 4.0×10^{-3} , and 3.9×10^{-3} , respectively for r , ρ , and τ . Consequently, we may consider the $f = 0.8$ and $f = 0.9$ statistically equivalent in essence.

When we relax the constraint $\beta = 0.6$, the improvement in the correlation is rather small: the smallest p-value for r decreases to 1.6×10^{-4} obtained for $(f = 0.75, \beta = 1.0)$, whereas the smallest p-values of ρ and τ become 2.2×10^{-3} for $(f = 0.9, \beta = 0.4)$. Therefore, admitting the possibility that β differs from the physically grounded value of 0.6 does not significantly improve the degree of correlation between V_f and L_{iso} . Consequently, hereafter we limit the discussion to the $\beta = 0.6$ case. Table 1 reports the correlation coefficients and p-values for all values of f , along with the number of GRBs with significant measures that were considered in each case.

The selection of $f = 0.8$ (or $f = 0.9$) as the best-correlation case is the result of a multitrial process, where the optimal value was selected out of 17 trial values for f in the range 0.1–0.9. On the one side, these are not completely independent, being due to different ways of processing the same LCs. On the other side, they are still the results of optimal selection from multiple attempts.

To determine the effective p-value, that is the probability that the observed degree of correlation is compatible with null hypothesis of no correlation, we carried out 10^4 simulations, each of which consisted in shuffling the array of peak luminosities and determining the best-correlation case for each synthetic sample of (V_f, L_{iso}) pairs in the very same way as we did for the real sample. Equal or lower p-values than the corresponding lowest real ones of (r, ρ, τ) were obtained in (26, 251, 232) cases: the effective p-values are, therefore, respectively 2.6×10^{-3} , 2.5%, and 2.3%. We conclude that the effective probability to obtain by accident an equally or more correlated sample in V_f – L_{iso} space than what shown in Fig. 3, under the null hypothesis of no correlation, is $\lesssim 2\%$, which is equivalent to the range 2.2–3.0 σ (Gaussian).

4.2. Comparison with past results

To compare the results with what was previously obtained by G05, we had to use the values obtained for $f = 0.45$, which was considered at the time. The resulting V_f – L_{iso} distribution is shown in Figure 4. Using this value for f , the sample of significant pairs (V_f, L_{iso}) decreases to 184 and the p-values of the linear and non-parametric correlation tests increase to 3.6% and 25%, respectively, so the previously found and very marginal evidence for correlation essentially vanishes. Table 3 reports all the values of V_f and L_{iso} for this sample.

The GRBs considered in G05 are 32: ignoring GRB 980425, which is a peculiar low-luminosity event (Kulkarni et al. 1998; Li & Chevalier 1999; Pian et al. 2000; Soderberg et al. 2004; Ghisellini et al. 2006), GRB 050603 whose redshift was later questioned (Hjorth et al. 2012), and other 5 *Swift*/BAT GRBs which are already included in the present sample, we are left with 25 additional GRBs from G05, adding which we end up with a sample of 209 GRBs, whose p-values are 4.7×10^{-3} (Pearson’s) and 3.8 and 4.1% for the other non-parametric tests. The luminosity values in G05 were calculated in the 100–1000 keV band, as originally done by R01. We then replaced their luminosity values with the broadband 1– 10^4 keV rest-frame analogues as reported in the literature as derived from broad-band spec-

Table 1. Correlation coefficients of the V_f – L_{iso} relation for the joint BAT-GBM sample, assuming $\beta = 0.6$.

f	Pearson's r	p-value (r)	Spearman's ρ	p-value (ρ)	Kendall's τ	p-value (τ)	$N_{\text{grb}}^{(a)}$
0.10	−0.085	0.41	−0.075	0.46	−0.052	0.45	99
0.15	0.055	0.55	0.021	0.82	0.012	0.84	124
0.20	−0.028	0.74	−0.033	0.7	−0.023	0.68	141
0.25	0.022	0.79	0.018	0.83	0.0072	0.9	151
0.30	0.06	0.45	0.046	0.56	0.029	0.59	158
0.35	0.16	0.037	0.097	0.21	0.066	0.2	170
0.40	0.14	0.063	0.08	0.29	0.056	0.27	177
0.45	0.15	0.036	0.086	0.25	0.057	0.25	184
0.50	0.2	0.0052	0.13	0.066	0.087	0.073	192
0.55	0.21	0.0038	0.15	0.032	0.1	0.036	195
0.60	0.2	0.0048	0.16	0.022	0.1	0.028	204
0.65	0.2	0.0038	0.18	0.01	0.11	0.015	207
0.70	0.23	0.00085	0.18	0.0078	0.12	0.011	208
0.75	0.24	0.00048	0.19	0.0053	0.12	0.0073	210
0.80	0.25	0.00031	0.19	0.0049	0.13	0.0057	212
0.85	0.24	0.00054	0.19	0.0051	0.13	0.0047	213
0.90	0.23	0.00085	0.2	0.004	0.13	0.0039	215

(a) Number of GRBs with 90%-significant estimates of V_f that were used in each case.

Table 2. Variability and peak luminosity for the joint BAT-GBM sample obtained assuming $f = 0.80$ and $\beta = 0.6$ (Figure 3). The four GRBs in the bottom are long-duration merger candidates and were treated separately.

GRB	z	T_f (s)	V_f	V_f 90% CI ^(a)	$\log L_{\text{iso}}$ (erg s^{-1})	Det ^(b) V_f	Ref ^(c) L_{iso}	$N_{\text{p}}^{(d)}$
050219A	0.2115	16.92 ± 1.08	0.069 ± 0.015	[0.044, 0.094]	49.991 ± 0.088	BAT	(1)	1
050315	1.949	48.86 ± 2.75	0.183 ± 0.021	[0.141, 0.210]	51.937 ± 0.165	BAT	(2)	3
050318	1.44	7.74 ± 0.33	0.204 ± 0.013	[0.183, 0.225]	51.839 ± 0.087	BAT	(2)	3
050401	2.9	13.05 ± 0.72	0.370 ± 0.015	[0.343, 0.390]	53.084 ± 0.091	BAT	(2)	4
050820A	2.6147	26.50 ± 1.87	0.224 ± 0.031	[0.177, 0.279]	53.136 ± 0.057	BAT	(3)	4

(a) 90% Confidence interval.

(b) Detector used to calculate V_f .

(c) References for L_{iso} : (1) Tsvetkova et al. (2021); (2) Yonetoku et al. (2010); (3) Tsvetkova et al. (2017); (4) present work; (5) Poolakkil et al. (2021) for GRBs before June 20, 2018; present work for later GRBs; (6) Frederiks et al. (2016); (7) Svinkin et al. (2016); (8) Frederiks et al. (2017); (9) Tsvetkova et al. (2018a); (10) Frederiks et al. (2018c); (11) Svinkin et al. (2018); (12) Frederiks et al. (2018a); (13) Frederiks et al. (2018b); (14) Tsvetkova et al. (2018b); (15) Tsvetkova et al. (2019); (16) Svinkin et al. (2019); (17) Frederiks et al. (2019); (18) Ridnaia et al. (2020); (19) Frederiks et al. (2020); (20) Frederiks et al. (2021a); (21) Svinkin et al. (2021); (22) Frederiks et al. (2021b); (23) Frederiks et al. (2021c); (24) Tsvetkova & Konus-Wind Team (2022); (25) Frederiks et al. (2023a); (26) Svinkin et al. (2024a); (27) Frederiks et al. (2023b); (28) Frederiks et al. (2024); (29) Svinkin et al. (2024b); (30) Yang et al. (2022); (31) Sun et al. (2023).

(d) Number of peaks with $S/N > 5$ taken from Guidorzi et al. (2024) and Maccary et al. (2024b).

troscopy. Compared with the G05 values, luminosities increased in most cases by a factor between 2 and 3.

In Appendix B we estimated a $\geq 3\%$ probability that the correlation assessed in G05 was accidental and caused by the poor sampling of the variability-luminosity space. On top of that, it is also possible that different selection effects between the joint sample of BAT-GBM of the present work and the early one of G05 also play a role: in particular, both GRB samples inevitably depend on the different suites of prompt optical followup facilities that enabled the afterglow identification and secured the redshift measurement.

4.3. Relation with the number of peaks

Figure 5 is the same as Figure 4, except for the colours which display the number of peaks of each GRB, N_{peaks} , as it was determined by us in Guidorzi et al. (2024) and in Maccary et al. (2024b) using MEPSA (Guidorzi 2015) and selecting peaks with $S/N > 5$.

The additional information supplied by N_{peaks} helps to characterise the GRBs with low V_f that were mostly missing in the early sample of G05 and which contributed to demote the correlation. Most GRBs with $V_f < 0.05$ have very few peaks (mainly 1 or 2) and are 25% of the whole sample. On average, these

Table 3. Similar to Table 2, apart from the value $f = 0.45$ (instead of $f = 0.80$ of Table 2), which was used to calculate V_f and which determines the sample of GRBs with significant V_f shown in Figures 4 and 5.

GRB	z	T_f (s)	V_f	V_f 90% CI ^(a)	$\log L_{\text{iso}}$ (erg s^{-1})	Det ^(b) V_f	Ref ^(c) L_{iso}	$N_p^{(d)}$
050219A	0.2115	7.56 ± 0.36	0.028 ± 0.014	[0.003, 0.051]	49.991 ± 0.088	BAT	(1)	1
050315	1.949	18.67 ± 1.10	0.072 ± 0.021	[0.038, 0.106]	51.937 ± 0.165	BAT	(2)	3
050318	1.44	3.49 ± 0.22	0.123 ± 0.013	[0.101, 0.144]	51.839 ± 0.087	BAT	(2)	3
050401	2.9	5.08 ± 0.72	0.177 ± 0.016	[0.148, 0.200]	53.084 ± 0.091	BAT	(2)	4
050820A	2.6147	9.94 ± 1.10	0.045 ± 0.016	[0.018, 0.070]	53.136 ± 0.057	BAT	(3)	4

(a) 90% Confidence interval.

(b) Detector used to calculate V_f .

(c) References for L_{iso} : (1) Tsvetkova et al. (2021); (2) Yonetoku et al. (2010); (3) Tsvetkova et al. (2017); (4) present work; (5) Poolakkil et al. (2021) for GRBs before June 20, 2018; present work for later GRBs; (6) Frederiks et al. (2016); (7) Svinkin et al. (2016); (8) Frederiks et al. (2017); (9) Tsvetkova et al. (2018a); (10) Frederiks et al. (2018c); (11) Svinkin et al. (2018); (12) Frederiks et al. (2018a); (13) Frederiks et al. (2018b); (14) Tsvetkova et al. (2018b); (15) Tsvetkova et al. (2019); (16) Svinkin et al. (2019); (17) Frederiks et al. (2019); (18) Ridnaia et al. (2020); (19) Frederiks et al. (2020); (20) Frederiks et al. (2021a); (21) Svinkin et al. (2021); (22) Frederiks et al. (2021b); (23) Frederiks et al. (2021c); (24) Tsvetkova & Konus-Wind Team (2022); (25) Frederiks et al. (2023a); (26) Svinkin et al. (2024a); (27) Frederiks et al. (2023b); (28) Frederiks et al. (2024); (29) Svinkin et al. (2024b); (30) Yang et al. (2022); (31) Sun et al. (2023).

(d) Number of peaks with $S/N > 5$ taken from Guidorzi et al. (2024) and Maccary et al. (2024b).

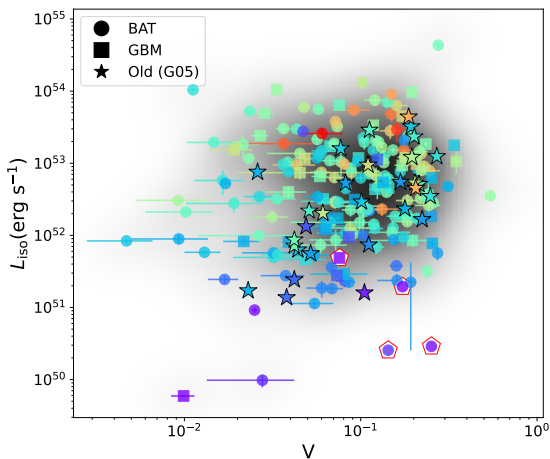


Fig. 4. Variability–luminosity correlation obtained for $f = 0.45$ and $\beta = 0.6$. In addition to the 184 GRBs analysed in the present work, also shown (stars) are GRBs from G05. Redshift is colour-coded. The shaded region shows a density map, obtained using a kernel density estimate, of the same data set (excluding the G05 GRBs). The four GRBs with red pentagons are long-duration merger candidates (GRB 060614, GRB 191019A, GRB 211211A, and GRB 230307A) that were considered separately.

low- V_f GRBs exhibit comparable luminosities with the complementary sample of more variable GRBs, except for a couple of them with $L_{\text{iso}} \lesssim 10^{50} \text{ erg s}^{-1}$. Figure 6 displays the LCs of five low- V_f GRBs, along with G05 GRB 000210⁹: all of them have $V_f \lesssim 0.03$, in line with a relatively smooth profile, and L_{iso} in the range 10^{52} – $10^{54} \text{ erg s}^{-1}$. Apart from some modulation in GRB 150314A, their profiles look like smooth, fast-rise exponential-decay (FRED) pulses: in principle, an external origin for their prompt emission cannot be excluded (a thorough

⁹ This *BeppoSAX* gamma-ray luminous and optically dark GRB is discussed in detail in Piro et al. (2002).

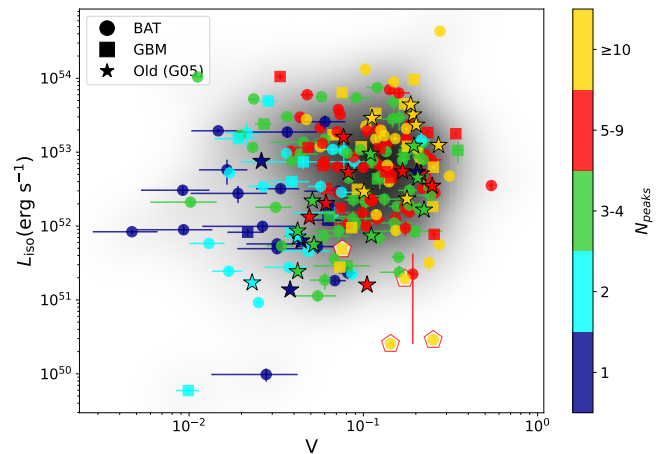


Fig. 5. Same plot as that of Figure 4, except for the colour-code, which corresponds to five different classes of number of peaks.

analysis of how tenable this scenario is for each of them, taking into account the corresponding afterglow multi-band data sets, is beyond the scope of the present work). Specifically, in the case of GRB 200829A an external origin has been put forward (Li et al. 2023), whereas Samuelsson et al. (2022) discuss a photospheric origin for GRB 150314A.

4.4. Long-duration merger candidates

Among the GRBs detected by either BAT or GBM, there are at least four credible long-duration merger candidates known to date: GRB 060614 (Della Valle et al. 2006; Fynbo et al. 2006), GRB 191019A (Levan et al. 2023), GRB 211211A (Yang et al. 2022; Troja et al. 2022), and GRB 230307A (Levan et al. 2024). Actually, one should also consider GRB 060505 (Fynbo et al. 2006): however, we ignored it because of the low S/N of BAT data along with its controversial nature (McBreen et al. 2008).

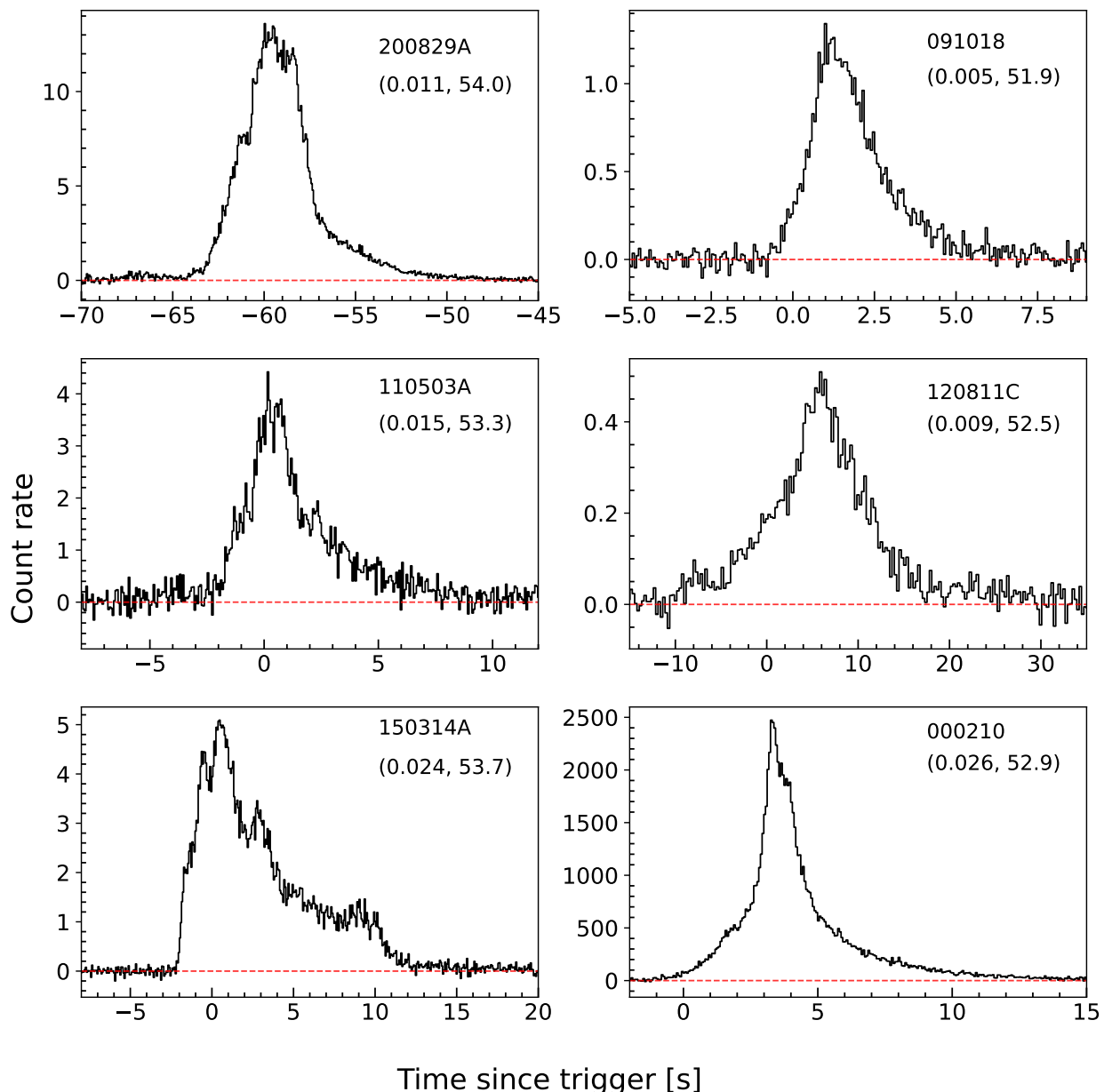


Fig. 6. Collection of 6 observer-frame GRBs with medium/high luminosity and low variability. Each panel reports the GRB name along with the $(V_f, \log L_{\text{iso}})$ pair. All of them are BAT bursts (15–150 keV), except for *BeppoSAX* GRB 000210 (40–700 keV) in the bottom right panel. In the case of BAT LCs, count rates are expressed in count s^{-1} per fully illuminated detector for an equivalent on-axis source.

Although they were not included in the samples for the statistical analysis of the V_f – L_{iso} correlation, we added them in Figures 4 and 5.

Two of them (GRB 060614 and GRB 191019A) lie within a region of their own: $V_f > 0.1$ and $L_{\text{iso}} < 10^{51}$ erg s^{-1} . GRB 211211A has comparable V_f , but higher L_{iso} (2×10^{51} erg s^{-1}), still lying in the outskirts of the distribution of standard long GRBs. Only GRB 230307A lies within a more densely populated region. All of them feature many peaks (ranging from 14 to 54), which contributed to the large values of V_f . That three out of four known candidates lie off the population distribution in the V_f – L_{iso} plane, suggests that the unusual combination of $V_f \gtrsim 0.1$ and $L_{\text{iso}} \lesssim 10^{51}$ erg s^{-1} might be a good indicator for a merger origin. In this respect, a possible closely related indicator was already tentatively identified in the MVT (Camisasca et al. 2023a,b; Veres et al. 2023).

To see whether there are other similar and as-yet disguised merger candidates, we explored the LC morphology of the GRBs that lie mostly in the high- V_f /low L_{iso} . Figure 7 displays a collection of 10 such GRBs, all of which share the following properties: $V_f > 0.1$ and $L_{\text{iso}} \lesssim 10^{52}$ erg s^{-1} s, with the only exception of 190719C ($L_{\text{iso}} = 3 \times 10^{52}$ erg s^{-1}) which has the highest V_f of all GRBs and whose projected offset seems to be more typical of a merger event and rather large for a collapsar event, although not unprecedented (Rossi et al. 2019). Among these 10 GRBs, there is a couple of them for which the collapsar identity was firmly established by the evidence for an associated SN: GRB 091127 (Cobb et al. 2010; Berger et al. 2011) and GRB 111228A (Klose et al. 2019). Yet, there are interesting events which look like short GRB with extended emission, such as GRB 161129A, as it was also noted by the *Swift* team: however, its nature remained inconclusive, given the spectral softness of the initial spike in

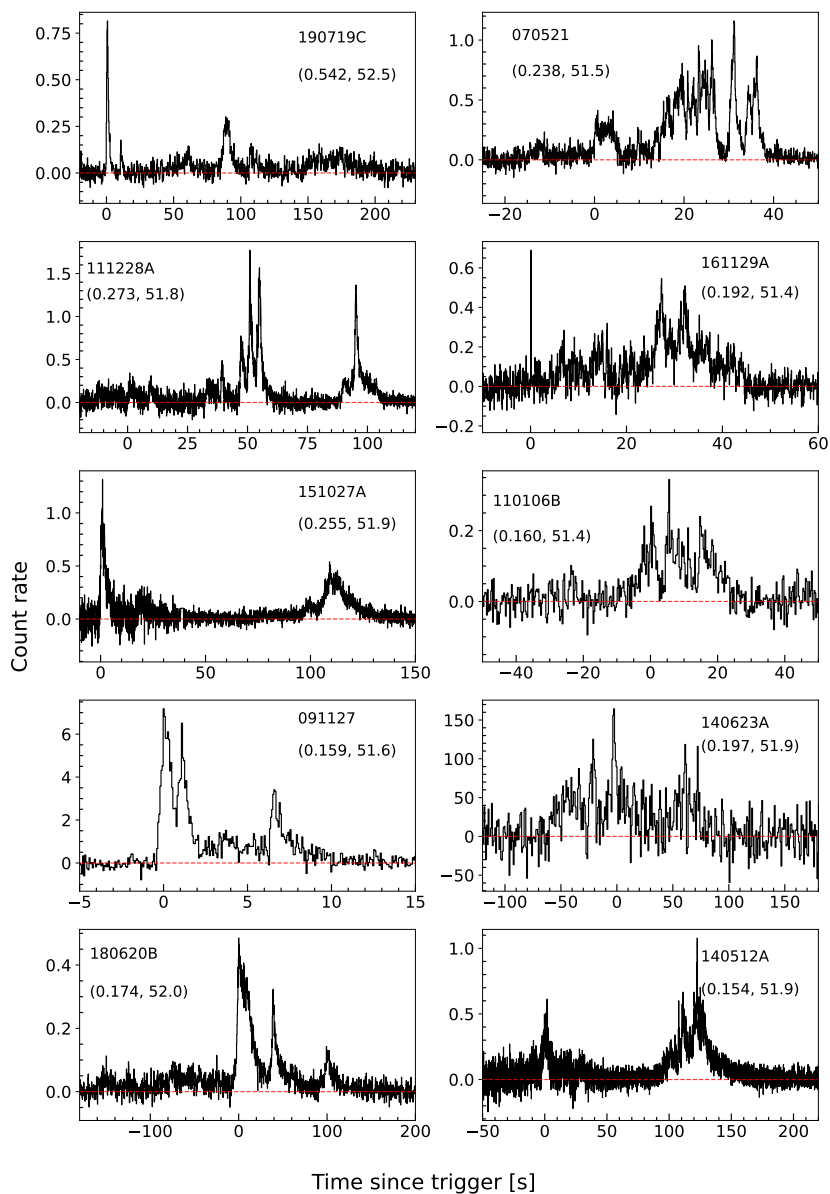


Fig. 7. Collection of 10 observer-frame GRBs with high variability, $V_f > 0.1$, and relatively low luminosity, $L_{\text{iso}} \lesssim 10^{52}$ erg s $^{-1}$. Each panel reports the GRB name along with the $(V_f, \log L_{\text{iso}})$ pair. All of them are BAT bursts (15–150 keV), except for *Fermi* GRB 140623A (8–900 keV). In the case of BAT LCs, count rates are expressed in count s $^{-1}$ per fully illuminated detector for an equivalent on-axis source.

comparison with the bulk population of short GRBs with and without extended emission (Barthelmy et al. 2016).

4.5. Variability and minimum variability timescale

Given that GRB time variability is a recurring general property that is often called for and interpreted in the literature, it is worth investigating and clarifying the relation between the definition of variability V_f considered in this work and the concept of MVT. To better illustrate this point, Figure 8 shows the two quantities calculated for a subsample of 184 GRBs. MVT values were either taken from or calculated as in Camisasca et al. (2023a). The two quantities are clearly neither independent nor tightly correlated. In fact, MVT identifies the shortest timescale over which a significant and uncorrelated flux variation is observed, irrespective of the overall properties of the whole LC, whereas V_f quantifies how much variance lies at short timescales with respect to long ones, where the short/long separation is dictated by the net time interval over which a sizeable fraction of energy is released (Section 3.1).

It is, therefore, no wonder that for $V_f \gtrsim 0.1$ all possible MVT values from 0.01 to ~ 30 s are observed: a high value of V_f does not necessarily imply the presence of narrow pulses, but it could also be obtained for a GRB featuring several broad peaks with different timescales and interspersed with quiescent times. Instead, most GRBs with $V_f \lesssim \text{few} \times 10^{-2}$ are inevitably missing narrow spikes, such that their MVT is \gtrsim a few seconds.

5. Discussion

Variable GRBs should arise when internal dissipation processes (e.g., internal shocks) occur outside the e^\pm pair photosphere, while X-ray rich bursts may arise from the processes occurring below it (Kobayashi et al. 2002; Mészáros et al. 2002). Let d and D be the width and separation of the random shells which characterise a GRB jet with velocity irregularity. The hydrodynamic timescale d/c and the angular spreading timescale D/c determine the rise and the decay time of a gamma-ray pulse, respectively. Since most observed pulses rise more quickly than they decay, the pulse width and pulse separation are mainly de-

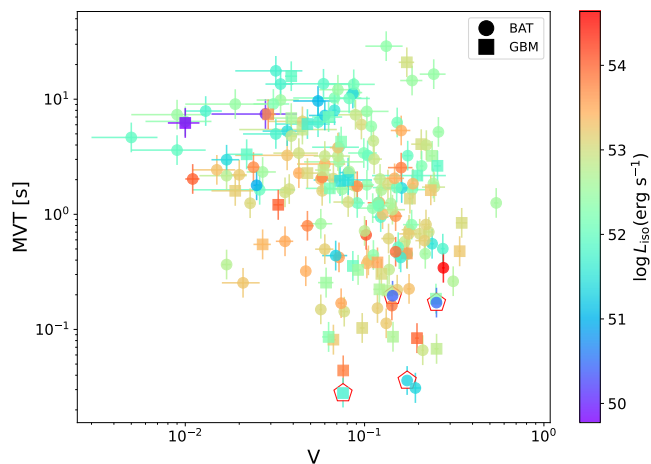


Fig. 8. MVT versus variability for a subsample of 184 GRBs. Pentagons are the four long-duration merger candidates. MVT values were calculated as in Camisasca et al. (2023a). Colour-coded is L_{iso} .

terminated by the angular spreading time D/c (Norris et al. 1996; Ryde & Petrosian 2002).

The distribution of peak separations¹⁰ $\{D/c\}$ for a GRB light curve usually has a large dispersion (Nakar & Piran 2002; Guidorzi et al. 2015). While the fastest variability timescale in a GRB can be as short as a few tens of milliseconds (Camisasca et al. 2023a), the largest peak separation or the total duration is usually much longer. Since shell collisions producing narrow pulses typically occur at small radii $\sim D\Gamma^2$, the photosphere might obscure these, leaving primarily the wider pulses visible. This will make the temporal profile smooth. If a jet has a smaller typical Lorentz factor, a larger fraction of the collisions occur at small radii $\sim D\Gamma^2$ below the photosphere; therefore, the smoothing effect is expected to be stronger.

The observed correlation between luminosity and variability in GRBs has been interpreted as reflecting a relation between the GRB jet’s opening angle and the mass involved in the explosion (Kobayashi et al. 2002). Since the beaming-corrected gamma-ray energy was believed to be narrowly clustered in the pre-*Swift* era, narrower jets would emit brighter gamma-ray emission. If narrower jets have typically higher Lorentz factors due to smaller mass loading, the photosphere could induce the luminosity and variability correlation. For the increased number of GRBs observed in the *Swift* era, it was found that the distribution of beaming-corrected gamma-ray energy is broader than previously thought, although still narrower than the distribution of isotropic energy (Liang et al. 2008).

The correlation between luminosity and variability is not significant for our larger sample of GRBs. To investigate potential indications of the photospheric effect in the GRB light curves, we test for a correlation between Lorentz factors and variability V_f , as slower jets might induce a stronger photospheric smoothing effect. However, we again find no significant correlations for the 37 GRBs, whose Lorentz factors were estimated from the afterglow onset times t_p (Ghirlanda et al. 2018). The p-values associated with linear and non-parametric correlation coefficients are 4 and 24%, respectively. This contrasts with MVT, which shows a negative correlation with the Lorentz factor, albeit with significant scatter: $\text{MVT} \propto \Gamma^{-2}$ (see fig. 13 of Camisasca et al. 2023a). This relation is consistent with the photospheric model in which MVT is determined by the curvature timescale at the

photosphere: $\text{MVT} \sim R_{\pm}/c\Gamma^2$, although the radii estimated from MVT and Γ are rather large, 10^{15-17} cm, for the photospheric radii R_{\pm} (Camisasca et al. 2023a; Kobayashi et al. 2002).

As shown in Fig. 8 and discussed in Section 4.5, the correlation between MVT and the variability V_f is very weak. The average power density spectrum (PDS) of very long GRBs (with $T_{90} > 100$ s) is known to follow a power-law distribution characterised by a slope $\alpha \sim -5/3$, featuring a clear break at about 1 Hz (Beloborodov et al. 2000; Guidorzi et al. 2012; Dichiara et al. 2013). Shorter GRBs exhibit PDS slopes that are more significantly influenced by statistical fluctuations. The lack of correlation between MVT and variability V_f can be attributed to the dominance of significant components in the light curve power spectrum at timescales substantially longer than the MVT (i.e., V_f is also determined by the pulses with longer timescales as well as by quiescent times). Considering MVT is better correlated with L_{iso} and Γ , it is likely to be more sensitive to the photospheric cut-off of the variability timescales; or, intrinsically the absolute measure of the short timescale with significant variance is correlated with them. If MVT is set by the photospheric effect, then the 1 Hz break in the averaged PDS should be due to the intrinsic nature of the central engine activity (i.e. the intrinsic separation distribution $\{D\}$).

A possible factor which weakens the correlation between Lorentz factors and variability V_f can be the separation distribution $\{D\}$ which can vary significantly between events intrinsically. Even if the average PDS follows the power-law, especially for events with a small number of peaks, the statistical fluctuations can be significant. If some events intrinsically lack narrowest components or longer-timescale components in the power spectrum dominate, their variability would be insensitive to the jet’s Lorentz factor and is always low. Another potential weakening factor is the errors in the estimates of Lorentz factors. Numerous collisions happen during an evolution of multiple shells. Each collision produces a pulse. However, the main pulses are produced by collisions between the fastest shells, $\sim \Gamma_{\text{max}}$, and the slowest shells, $\sim \Gamma_{\text{min}}$. Such a collision happens at $R \sim \Gamma_{\text{min}}^2 D_i$ for an initial separation D_i . The suppression of narrow peaks and consequent smoothing effect basically depend on how much the photosphere radius R_{\pm} is larger than $\Gamma_{\text{min}}^2 D_{\text{min}}$. The Lorentz factor based on the afterglow onset time gives a characteristic value after the internal dissipation process is settled, but it might not correlate with the minimal value Γ_{min} of the intrinsic distribution well.

In addition, it is also possible that the presence of GRBs, whose prompt emission has a completely different origin, contributed to weaken the possible correlation between V_f and L_{iso} . Specifically, this could be the case of low- V_f GRBs, having just one broad peak and with a typical L_{iso} : their prompt emission might have an external origin, marking the high-energy afterglow onset (Section 4.3 and Fig. 5). For five of the six external-shock GRB candidates shown in Fig. 6, the upper limits of the afterglow onset time t_p are available (see Table 4). We find tight upper limits especially for four of these events. The afterglow onset could happen right after/during the prompt gamma-ray emission, or the prompt gamma-ray emission itself could be the afterglow onset as we propose the external shock origin. Interestingly, two of these events (GRB 091018 and GRB 120811C) have very low E_p : taking the E_p distribution of the merged sample of 317 GRBs from Tsvetkova et al. (2017, 2021), only 1 ($\sim 0.3\%$) and 33 (10%) have equal or smaller E_p than those two bursts, respectively.

Finally, in Section 4.4 and in Figure 4 we showed that three out of four known long-duration compact binary merger candi-

¹⁰ Also known as waiting times.

Table 4. Upper limits on the observed afterglow onset time t_p , prompt duration T_{90} , and peak energy E_p of the time-integrated νF_ν spectrum for 5 external-shock GRB candidates shown in Fig. 6.

GRB	T_{90} (s)	t_p (s)	E_p (keV)
091018	4.4	< 138	27^{+2}_{-4}
110503A	58.7	< 275	220 ± 12
120811C	24.3	< 1020	49 ± 3
150314A	14.8	< 135	350 ± 10
200829A	13.0	< 100	336 ± 11

Notes. Upper limits on the afterglow onset times are from Ghirlanda et al. (2018) and Li et al. (2023). Peak energies are from Tsvetkova et al. (2017, 2021); Ridnaia et al. (2020). All values refer to the observer frame.

dates lie off the bulk of long GRBs, in the region with $V_f > 0.1$ and $L_{\text{iso}} < 10^{51}$ erg s $^{-1}$, with the fourth, GRB 230307A, lying closer to other typical long GRBs. Additionally, considering their MVT (Fig. 8 and Camisasca et al. 2023a), these events appear to be characterised by the rare combination of a very small MVT (a few ten ms), high variability, and relatively low luminosity. We tentatively identified other interesting events, displayed in Fig. 7, with analogous features: although for a couple of them an associated SN was found, the remaining candidates might be worth a deeper investigation.

6. Conclusions

Twenty years after the launch of *Swift* and its subsequent enhancement by *Fermi*, the number of GRBs with measured redshifts has significantly increased. This growth necessitates a new, more statistically robust examination of the variability–luminosity relation. Previously, this relation was reported based on a sample of approximately 30 GRBs available a few years after the initial afterglow discoveries.

The aim of this study is testing the correlation by utilising the extensive data sets available today. Using a sample of 216 GRBs detected by *Swift*, *Fermi*, and *Konus/WIND*, each with robust estimates for both variability V_f and isotropic-equivalent peak luminosity L_{iso} , we found that the scatter has increased to such an extent that the correlation can no longer be considered statistically significant (p-value $\lesssim 2\%$).

The definition of V_f adopted in this study, originally provided by R01, measures the temporal power of short-to-intermediate timescales with respect to the total power, which includes the contribution from all timescales. This definition of V_f is not to be confused with that of MVT (MacLachlan et al. 2013; Golkhou & Butler 2014; Golkhou et al. 2015; Camisasca et al. 2023a), another observable used to characterise GRB variability. MVT corresponds to the shortest timescale over which a statistically significant and uncorrelated flux change is observed, regardless of the power in long timescales. Here, we investigated for the first time the relation between V_f and MVT and found a weak correlation (Fig. 8). This finding helps explain why MVT is found to anti-correlate with L_{iso} and the Lorentz factor Γ (measured from the afterglow onset time), despite significant scatter (Camisasca et al. 2023a), while V_f does not.

When internal dissipation occurs within the e^\pm photosphere, the resulting gamma-ray light curve is smoothed out. Narrower pulses, produced at smaller radii, are particularly sensitive to this photospheric cut-off. The stronger correlation of L_{iso} and Γ with MVT compared to V_f suggests that V_f is mainly influenced by pulses and quiescent periods with timescales much longer than

the MVT scale. MVT might be determined by the photospheric effect or it is intrinsically correlated with L_{iso} and Γ due to the unknown nature of the central engine.

Furthermore, we identified several GRBs with a single broad and smooth peak, low V_f and typical L_{iso} , whose origin may be attributed to external shocks, differing from the majority of the observed GRBs (Fig. 6). This scenario is supported by the tight upper limits on the afterglow onset times determined from early optical afterglow observations. Notably, the prompt emissions of two of them (GRB 091018 and GRB 120811C) are very soft, having peak energies of the time-average νF_ν spectrum in the low tail of the observed population.

Lastly, the combination of high variability ($V_f > 0.1$), relatively low luminosity ($L_{\text{iso}} < 10^{51}$ erg s $^{-1}$), and short MVT ($\lesssim 0.1$ s; Camisasca et al. 2023a) appears to be a promising indicator for a compact binary merger origin, despite the long duration and deceptive time profile. We have tentatively identified other potential candidates with similar characteristics.

Acknowledgements. D.F., A.L., A.R., D.S., M.U. acknowledge financial support from the basic funding program of the Ioffe Institute FFUG-2024-0002. A.T. acknowledges financial support from “ASI-INAF Accordo Attuativo HERMES Pathinder operazioni n. 2022-25-HH.0” (discussion of the results, editing the paper) and the basic funding program of the Ioffe Institute FFUG-2024-0002 (computation of L_{iso}). L.F. acknowledges support from the AHEAD-2020 Project grant agreement 871158 of the European Union’s Horizon 2020 Program. We thank the reviewer for their detailed and constructive report.

References

- Abbott, B. P., Abbott, R., Abbott, T. D., et al. 2017, *ApJ*, 848, L13
Band, D., Matteson, J., Ford, L., et al. 1993, *ApJ*, 413, 281
Barthelmy, S. D., Cummings, J. R., Gehrels, N., et al. 2016, *GRB Coordinates Network*, 20220, 1
Beloborodov, A. M., Stern, B. E., & Svensson, R. 2000, *ApJ*, 535, 158
Berger, E., Chornock, R., Holmes, T. R., et al. 2011, *ApJ*, 743, 204
Blinnikov, S. I., Novikov, I. D., Perevodchikova, T. V., & Polnarev, A. G. 1984, *Soviet Astronomy Letters*, 10, 177
Camisasca, A. E., Guidorzi, C., Amati, L., et al. 2023a, *A&A*, 671, A112
Camisasca, A. E., Guidorzi, C., Bulla, M., et al. 2023b, *GRB Coordinates Network*, 33577, 1
Cobb, B. E., Bloom, J. S., Perley, D. A., et al. 2010, *ApJ*, 718, L150
Della Valle, M., Chincarini, G., Panagia, N., et al. 2006, *Nature*, 444, 1050
Dichiara, S., Guidorzi, C., Amati, L., & Frontera, F. 2013, *MNRAS*, 431, 3608
Dichiara, S., Tsang, D., Troja, E., et al. 2023, *ApJ*, 954, L29
Eichler, D., Livio, M., Piran, T., & Schramm, D. N. 1989, *Nature*, 340, 126
Eyles-Ferris, R. A. J., Nixon, C. J., Coughlin, E. R., & O’Brien, P. T. 2024, *ApJ*, 965, L20
Fenimore, E. E. & Ramirez-Ruiz, E. 2000, *ArXiv Astrophysics e-prints* [astro-ph/0004176]
Fenimore, E. E., Ramirez-Ruiz, E., & Wu, B. 1999, *ApJ*, 518, L73
Frederiks, D., Golenetskii, S., Aptekar, R., et al. 2018a, *GRB Coordinates Network*, 23011, 1
Frederiks, D., Golenetskii, S., Aptekar, R., et al. 2018b, *GRB Coordinates Network*, 23061, 1
Frederiks, D., Golenetskii, S., Aptekar, R., et al. 2019, *GRB Coordinates Network*, 26576, 1
Frederiks, D., Golenetskii, S., Aptekar, R., et al. 2020, *GRB Coordinates Network*, 29084, 1
Frederiks, D., Golenetskii, S., Aptekar, R., et al. 2016, *GRB Coordinates Network*, 20059, 1
Frederiks, D., Golenetskii, S., Aptekar, R., et al. 2017, *GRB Coordinates Network*, 20995, 1
Frederiks, D., Golenetskii, S., Aptekar, R., et al. 2018c, *GRB Coordinates Network*, 22546, 1
Frederiks, D., Golenetskii, S., Lysenko, A., et al. 2021a, *GRB Coordinates Network*, 30196, 1
Frederiks, D., Golenetskii, S., Lysenko, A., et al. 2021b, *GRB Coordinates Network*, 30366, 1
Frederiks, D., Golenetskii, S., Lysenko, A., et al. 2021c, *GRB Coordinates Network*, 30694, 1
Frederiks, D., Lysenko, A., Ridnaia, A., et al. 2023a, *GRB Coordinates Network*, 34511, 1

- Frederiks, D., Lysenko, A., Ridnaia, A., et al. 2023b, GRB Coordinates Network, 35377, 1
- Frederiks, D., Lysenko, A., Ridnaia, A., et al. 2024, GRB Coordinates Network, 35701, 1
- Fynbo, J. P. U., Watson, D., Thöne, C. C., et al. 2006, *Nature*, 444, 1047
- Gehrels, N., Chincarini, G., Giommi, P., et al. 2004, *ApJ*, 611, 1005
- Gehrels, N., Norris, J. P., Barthelmy, S. D., et al. 2006, *Nature*, 444, 1044
- Ghirlanda, G., Nappo, F., Ghisellini, G., et al. 2018, *A&A*, 609, A112
- Ghisellini, G., Ghirlanda, G., Merghetti, S., et al. 2006, *MNRAS*, 372, 1699
- Goldstein, A., Cleveland, W. H., & Kocevski, D. 2022, *Fermi GBM Data Tools: v1.1.1*
- Golkhou, V. Z. & Butler, N. R. 2014, *ApJ*, 787, 90
- Golkhou, V. Z., Butler, N. R., & Littlejohns, O. M. 2015, *ApJ*, 811, 93
- Gompertz, B. P., Rasio, M. E., Nicholl, M., et al. 2023, *Nature Astronomy*, 7, 67
- Guidorzi, C. 2015, *Astronomy and Computing*, 10, 54
- Guidorzi, C., Dichiara, S., Frontera, F., et al. 2015, *ApJ*, 801, 57
- Guidorzi, C., Frontera, F., Montanari, E., et al. 2005, *MNRAS*, 363, 315
- Guidorzi, C., Frontera, F., Montanari, E., et al. 2006, *MNRAS*, 371, 843
- Guidorzi, C., Lacapra, M., Frontera, F., et al. 2011, *A&A*, 526, A49
- Guidorzi, C., Margutti, R., Amati, L., et al. 2012, *MNRAS*, 422, 1785
- Guidorzi, C., Sartori, M., Maccary, R., et al. 2024, *A&A*, 685, A34
- Hjorth, J., Malesani, D., Jakobsson, P., et al. 2012, *ApJ*, 756, 187
- Kaneko, Y., Preece, R. D., Briggs, M. S., et al. 2006, *ApJS*, 166, 298
- Kimura, S. S. 2023, in *The Encyclopedia of Cosmology. Set 2: Frontiers in Cosmology. Volume 2: Neutrino Physics and Astrophysics*, ed. F. W. Stecker, 433–482
- Klose, S., Schmidl, S., Kann, D. A., et al. 2019, *A&A*, 622, A138
- Kobayashi, S., Ryde, F., & MacFadyen, A. 2002, *ApJ*, 577, 302
- Kulkarni, S. R., Frail, D. A., Wieringa, M. H., et al. 1998, *Nature*, 395, 663
- Lesage, S., Veres, P., Briggs, M. S., et al. 2023, *ApJ*, 952, L42
- Levan, A. J., Gompertz, B. P., Salafia, O. S., et al. 2024, *Nature*, 626, 737
- Levan, A. J., Malesani, D. B., Gompertz, B. P., et al. 2023, *Nature Astronomy*, 7, 976
- Li, J., Lin, D.-B., Lu, R.-J., et al. 2023, *ApJ*, 944, 21
- Li, Z.-Y. & Chevalier, R. A. 1999, *ApJ*, 526, 716
- Liang, E.-W., Racusin, J. L., Zhang, B., Zhang, B.-B., & Burrows, D. N. 2008, *ApJ*, 675, 528
- Lien, A., Sakamoto, T., Barthelmy, S. D., et al. 2016, *ApJ*, 829, 7
- Maccary, R., Guidorzi, C., Amati, L., et al. 2024a, *ApJ*, 965, 72
- Maccary, R., Maistrello, M., Guidorzi, C., et al. 2024b, *A&A*, 688, L8
- MacFadyen, A. I. & Woosley, S. E. 1999, *ApJ*, 524, 262
- MacLachlan, G. A., Shenoy, A., Sonbas, E., et al. 2013, *MNRAS*, 432, 857
- MacLachlan, G. A., Shenoy, A., Sonbas, E., et al. 2012, *MNRAS*, 425, L32
- McBreen, S., Foley, S., Watson, D., et al. 2008, *ApJ*, 677, L85
- Mészáros, P. 2017, in *Neutrino Astronomy: Current Status, Future Prospects*, ed. T. Gaisser & A. Karle, 1–14
- Mészáros, P., Ramirez-Ruiz, E., Rees, M. J., & Zhang, B. 2002, *ApJ*, 578, 812
- Murase, K. & Bartos, I. 2019, *Annual Review of Nuclear and Particle Science*, 69, 477
- Nakar, E. & Piran, T. 2002, *MNRAS*, 331, 40
- Narayan, R., Paczynski, B., & Piran, T. 1992, *ApJ*, 395, L83
- Nava, L. 2021, *Universe*, 7, 503
- Noda, K. & Parsons, R. D. 2022, *Galaxies*, 10, 7
- Norris, J. P. & Bonnell, J. T. 2006, *ApJ*, 643, 266
- Norris, J. P., Nemiroff, R. J., Bonnell, J. T., et al. 1996, *ApJ*, 459, 393
- Paczynski, B. 1991, *Acta Astron.*, 41, 257
- Paczynski, B. 1998, *ApJ*, 494, L45
- Pian, E., Amati, L., Antonelli, L. A., et al. 2000, *ApJ*, 536, 778
- Piro, L., Frail, D. A., Gorosabel, J., et al. 2002, *ApJ*, 577, 680
- Planck Collaboration, Aghanim, N., Akrami, Y., et al. 2020, *A&A*, 641, A6
- Poolakkil, S., Preece, R., Fletcher, C., et al. 2021, *ApJ*, 913, 60
- Preece, R., Burgess, J. M., von Kienlin, A., et al. 2014, *Science*, 343, 51
- Preece, R. D., Briggs, M. S., Malozzi, R. S., et al. 2000, *ApJS*, 126, 19
- Press, W. H., Teukolsky, S. A., Vetterling, W. T., & Flannery, B. P. 1992, *Numerical recipes in C. The art of scientific computing*
- Racusin, J. L., Karpov, S. V., Sokolowski, M., et al. 2008, *Nature*, 455, 183
- Reichart, D. E., Lamb, D. Q., Fenimore, E. E., et al. 2001, *ApJ*, 552, 57
- Ridnaia, A., Golenetskii, S., Aptekar, R., et al. 2020, GRB Coordinates Network, 28323, 1
- Rossi, A., Heintz, K. E., Fynbo, J. P. U., et al. 2019, GRB Coordinates Network, 25252, 1
- Ryde, F. & Petrosian, V. 2002, *ApJ*, 578, 290
- Sakamoto, T., Sato, G., Barbier, L., et al. 2009, *ApJ*, 693, 922
- Samuelsson, F., Lundman, C., & Ryde, F. 2022, *ApJ*, 925, 65
- Soderberg, A. M., Kulkarni, S. R., Berger, E., et al. 2004, *Nature*, 430, 648
- Sonbas, E., MacLachlan, G. A., Dhuga, K. S., et al. 2015, *ApJ*, 805, 86
- Sun, H., Wang, C. W., Yang, J., et al. 2023, arXiv e-prints, [arXiv:2307.05689](https://arxiv.org/abs/2307.05689)
- Svinkin, D., Frederiks, D., Lysenko, A., et al. 2024a, GRB Coordinates Network, 35893, 1
- Svinkin, D., Frederiks, D., Lysenko, A., et al. 2024b, GRB Coordinates Network, 35758, 1
- Svinkin, D., Golenetskii, S., Aptekar, R., et al. 2016, GRB Coordinates Network, 20197, 1
- Svinkin, D., Golenetskii, S., Aptekar, R., et al. 2019, GRB Coordinates Network, 24015, 1
- Svinkin, D., Golenetskii, S., Aptekar, R., et al. 2018, GRB Coordinates Network, 22825, 1
- Svinkin, D., Golenetskii, S., Frederiks, D., et al. 2021, GRB Coordinates Network, 30276, 1
- Troja, E., Fryer, C. L., O'Connor, B., et al. 2022, *Nature*, 612, 228
- Tsvetkova, A., Frederiks, D., Golenetskii, S., et al. 2017, *ApJ*, 850, 161
- Tsvetkova, A., Frederiks, D., Svinkin, D., et al. 2021, *ApJ*, 908, 83
- Tsvetkova, A., Golenetskii, S., Aptekar, R., et al. 2018a, GRB Coordinates Network, 22513, 1
- Tsvetkova, A., Golenetskii, S., Aptekar, R., et al. 2018b, GRB Coordinates Network, 23363, 1
- Tsvetkova, A., Golenetskii, S., Aptekar, R., et al. 2019, GRB Coordinates Network, 23637, 1
- Tsvetkova, A. & Konus-Wind Team. 2022, GRB Coordinates Network, 31436, 1
- Tsvetkova, A., Svinkin, D., Karpov, S., & Frederiks, D. 2022, *Universe*, 8, 373
- Veres, P., Bhat, P. N., Burns, E., et al. 2023, *ApJ*, 954, L5
- Woosley, S. E. 1993, *ApJ*, 405, 273
- Yang, J., Ai, S., Zhang, B. B., et al. 2022, *Nature*, 612, 232
- Yonetoku, D., Murakami, T., Tsutsui, R., et al. 2010, *PASJ*, 62, 1495
- Yoon, S. C. & Langer, N. 2005, *A&A*, 443, 643

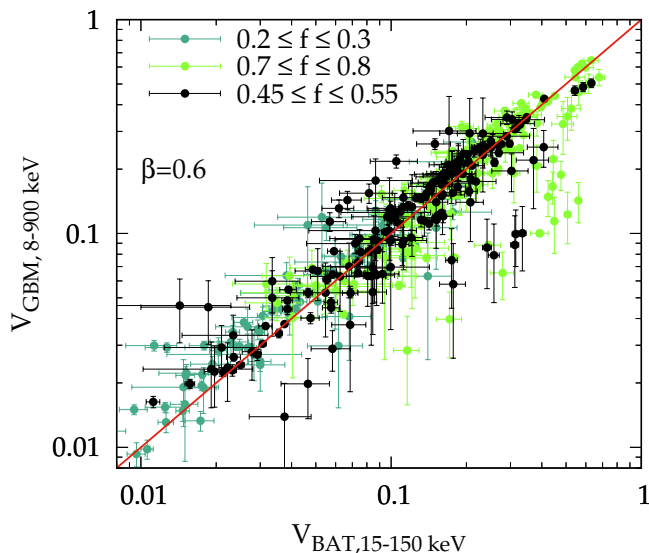


Fig. A.1. Comparison between estimates of variability obtained with BAT in the 15–150 keV band vs. the GBM estimates in the 8–900 keV band, obtained for a common sample with significant measures of variability. Three different ranges for f are shown.

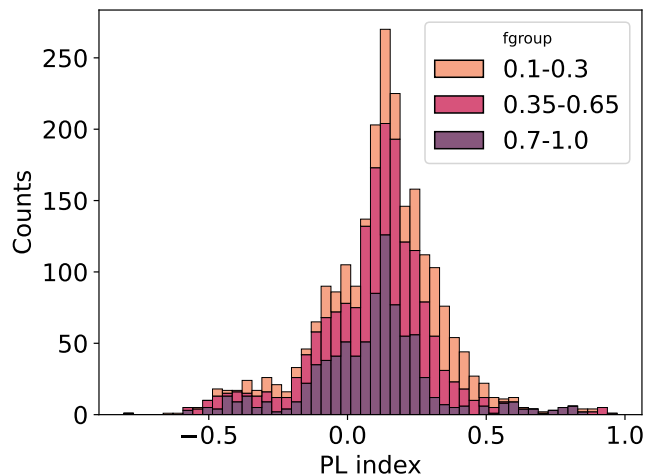


Fig. A.2. Distributions of the PL index α that models the dependence of variability on photon energy as $V \propto E^\alpha$ for a sample of 44 GRB shared by BAT and GBM having significant measures of V_f for all of the three energy passbands (15–150, 8–150, and 150–900 keV). The three stacked histograms refer to three different ranges for f .

Appendix A: Dependence of variability on energy passband

The analysis of a common sample of BAT-GBM GRBs having significant measures of V_f for each of the three energy passbands (15–150, 8–150, and 150–900 keV) showed that in most cases there is a weak dependence of V_f on the energy passband. Figure A.1 shows the comparison of V_f obtained from the total-passband light curves of the two detectors. Unlike Figure 2, which is limited to the $f = 0.45$ case, Fig. A.1 shows all values of f (see Section 3.1 for a definition of f).

By assuming, for each energy channel, the geometric mean E of its boundary values and fitting the three points of each GRB and each combination of f and β values with a power-law, $V \propto E^\alpha$, we obtained an acceptable fit for 82% of cases. The corresponding α distribution is shown in Figure A.2 for three

different ranges of f . Most values differ from zero by a relatively small amount, with a median value $\alpha_{\text{med}} = 0.13$ and [0.0, 0.24] as interquartile range, when all values of f are included.

We used this result to study the impact of using the two measures of V_f obtained with the full passbands of both BAT and GBM interchangeably: we derived the distribution of the ratio ξ between V_f calculated at 47 keV and V_f calculated at 85 keV, corresponding to the geometric mean energy of the 15–150 and of the 8–900 keV passbands, respectively. The median value is $\xi_{\text{med}} = 1.08$, with 0.82 and 1.24 as the 5% and 95% quantiles, respectively. This can be summarised as a $\lesssim 20\%$ discrepancy for most measures of V_f obtained with BAT and with GBM.

Appendix B: Comparison and test with past results

As anticipated in Section 4.2, we concluded that the correlation between L_{iso} and V_f that was found in the early years by R01 and confirmed by G05 was possibly an artefact caused by the poor sampling of the $L_{\text{iso}}-V_f$ space.

Here we investigate the reason why the evidence for correlation was stronger for the smaller sample of G05: this is easily understood by looking at Figure B.1: in the region with low V_f and high L_{iso} there is only one old GRB (000210). It is possible to identify a power-law (dashed line) below which all old GRBs but 000210 lie: $L_{\text{iso}} = (3 \times 10^{49} \text{ erg s}^{-1}) (V_f/0.006)^{3.8}$. The slope of this power-law, 3.8, is also consistent with the slope $3.3^{+1.1}_{-0.9}$ that was found by R01 to describe the relation between L_{iso} and V_f . Assuming that the distribution of the old G05 GRBs in the V_f-L_{iso} space is the same as the one of BAT and GBM GRBs, we estimated the probability that all of the 25, except for one at most, lie on the same side of the power-law by accident: 42/184 from the joint BAT-GBM sample lie above the boundary power-law. Assuming $p = 42/184 = 22.8\%$ as the probability for a single GRB to lie on the left side, the corresponding odds that at least 24 out of 25 lie on the same side of the dividing line are easily calculated with a two-sided binomial test¹¹ and are 3%, so not impossible. Also, considering that the dividing line was found a posteriori, the correct odds are likely somewhat greater. In fact, a Kolmogorov-Smirnov 2-D test¹² in the $\log V_f-\log L_{\text{iso}}$ plane between our set and the G05 one yields a p-value of 21%, which confirms the absence of evidence for a different parent distribution.

We conclude that stronger evidence for the V_f-L_{iso} correlation that was found in the early years was the result of a poor sampling of the V_f-L_{iso} plane.

¹¹ We used the `scipy.stats.binomtest` function.

¹² The function `ks2d2s` from Press et al. (1992) was used.

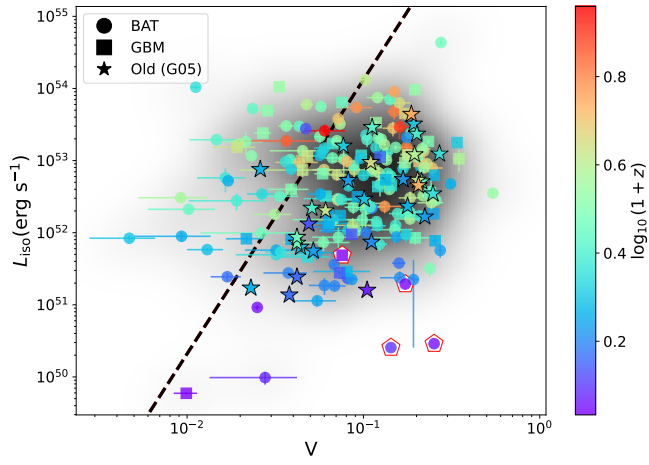


Fig. B.1. Same as Figure 4 with an additional dashed line that shows the region below which all but one old points lie.